Volume 68(3). Published December, 01, 2019
www.jnsciences.org
E-ISSN 2286-5314

Computed Tomography And Magnetic Resonance Imaging of The Brain And Associated Structures Of The One Humped Camel (*Camelusdromedarius*): a comparative study

ABDELMONEME BEN KHALIFA[1*], JABER BELKHIRIA[2], HBIBA HAMDI[1], BALKISDAKHLI[1], WALID CHANDOUL[3]AND ABDELHAMID MATTOUSSI[1]

[1]Department of Anatomy and Embryology, National School of Veterinary Medicine, SidiThabet Tunisia
[2] School of Veterinary Medicine, University of California, USA
[3]District of Animal Production Of Medenine Tunisia

*Corresponding author: benkhalifaabdelmonem@gmail.com

Abstract – We aimed to compare two medical imaging techniques; computed tomographyand magnetic resonance imaging in the exploration of various anatomical components of the brain and its associated structures in the dromedary.
A total of four healthy dromedary heads were used; two heads underwent anatomical sections; two other heads were imaged respectively by computed tomography and by magnetic resonance imaging. We selected eight snapshots of each of the techniques that gave excellent correspondence with the anatomical sections. Magnetic resonance images were characterized by their excellent contrast between gray and white matter and ventricles. They allowed us to identify the majority of the brain's structures. Computed tomography images provide good differentiation between bones and soft tissues of the head. This comparative analysis demonstrates that magnetic resonance imaging is clearly superior to computed tomography in identifying key brain elements.
These computed tomography and magnetic resonance images are intended to be a useful anatomical tool in the interpretation of clinical imaging studies of the encephalon and associated structures in camels.

Key words: anatomy; cross sections; dromedary; encephalon; imaging techniques

1. Introduction

Veterinary medical imaging has rapidly improved since the end of the 20th century. It plays now an essential role in veterinary scientific research and diagnostic procedures. In fact, modern diagnostic imaging techniques, such as computed tomography (CT) and magnetic resonance imaging (MRI) enable us to produce images of body sections in different planes with good anatomical resolution and high contrast between structures.
Anatomical exploration of the dromedary's head through the assessment of its structure, soft tissues, and oral and nasal cavities is difficult due to their complex anatomical organizations (Blanco et al. 2015).Physical exploration and classical imager such as radiography and ultrasound provide limited information on its anatomical structure (Osuobeni and Hamid Zada 1999; Byers et al. 2007).
Throughout this study, we aimed to compare the respective contributions of MRI and CT for the identification of the different components of the normal dromedary brain and its associated structures using an atlas of MRI, CT and macroscopic sections images. These CT and MRI images are intended to be a useful anatomic reference for clinical studies of the head in dromedary.

2. Materials and methods

We used four dromedary heads belonging to adult subjects free from any apparent nervous pathology. These heads were collected directly from two slaughterhouses. We chose slaughterhouses closest to imaging centers to minimize post-mortem changes. Immediately after slaughter, each head was separated from the body at the atlanto-occipital joint.
We performed anatomical cuts using an electric band saw on the first two samples after freezing. We performed seven transverse sections spaced 15 mm apart, from the internal angle of the eye to the

atlanto-occipital joint on the first head and a sagittal section passing through the median plane on the second. The surface of each sectional plane was cleaned, dissected and photographed.
The third head was transferred for a CT scan at the center of radiological, ultrasonic and nuclear medicine exploration of Tunis immediately after slaughter. The device used is a multi-cut scanner General Electric Helical Type. The CT scan enabled us to acquire successive sections; spaced 0.6 mm apart. Those fine and joined sections allow a good spatial resolution and thus a better discrimination between small structures. We chose eight images out of the tomodensitometric sections.
We sent the fourth and final sample to the radiology center at the Amal Polyclinic in Zarzis, southern Tunisia, for MRI. The machine used is a 3 Tesla high-field MRI, General Electric Model Signa, with superconducting magnet and a human head coil. Transverse images were obtained perpendicular to the soft palate to provide a reference for slice orientation (Arencibia et al. 2005). Dromedary's head MRI allowed us to have successive series of images according to the different weights T1, T2 and T2 FLAIR. We chose the T1 weighting because it is the best weighting for the anatomical study of the brain (Mogicato et al. 2011; De Rycke 2007). Among the images obtained, we selected eight images corresponding to anatomical sections of the brain.
Anatomical structures were identified and captioned on all anatomical sections as well as on corresponding CT and MRI images thanks to the confrontation of numerous structures in accordance with N.A.V (NominaAnatomicaVeterinaria 2012).

3. Results and discussions

3.1. Macroscopic cross sections

Via the transverse anatomical sections of the head, we were able to examine the encephalon and its deepest structures at an interval of 1.5 cm. Both cross (seven in total) and median sections show the topography of the brain and its relationship to the neighbouringstructures such as the cranial bones and surrounding soft tissues.
Anatomically, the forebrain includes the diencephalon and telencephalon. The latter is formed of two cerebral hemispheres separated by the interhemispheric fissure (Figure 2/8, 4/6, 5/5) and connected by the corpus callosum (Figure 3/8, 4/7, 5/6). This latter, forms the roof of the lateral ventricles (Figure 4/10, 5/7).
The corpus callosum is thick compared to the size of the cerebral hemispheres. Each hemisphere is composed of the gray matter which forms the cerebral cortex. The white substance, however, has a striated appearance due to the afferent and efferent fibers, ventrally bordering a voluminous gray body referred to as the striatum.
The striatum is the large basal nucleus of the hemisphere located at a rostral level of the thalamus. It is crossed by a large internal capsule which divides it into a caudate nucleus and putamen (Figure 3/11). A thin layer of white substance, the outer capsule, separates it from the claustrum, an elongated and fine band of gray substance.
The caudate nucleus (Figure 3/9) is a large gray mass forming the floor of the lateral ventricle.
The diencephalon is located ventrally in transverse sections and consists of the epithalamus, thalamus, metathalamus and hypothalamus.
The thalamus (Figure 4/8) is the largest part of the diencephalon. A considerable part of interthalamic adhesion forms the floor of the lateral ventricle. The hypothalamus (Figure 4/13) forms the floor and lateral walls of the third ventricle (Figure 4/9, 5/8) and leads to the optic chiasm. The latter and the optic nerve (Figure 2/9, 3/13) are clearly visible under the thalamus.
The meninges were identified only on the median section (Figure 8/25) whereas on the cross sections we were not able to identify them.
In our study, cross-sectional anatomical sections were made with a spacing of about 1.5 cm. It was not possible to obtain finer cuts because the band saw used did not allow it despite the fact that the head was well frozen. A weaker space might have enabled us to visualize more anatomical structures. Also, having paramedian and dorsal anatomical sections could have given us better details about the topography and the reports of the brain.

3.2. Computed tomography

3.2.1. Brain

The brain and surrounding structures are obvious; the encephalon was opaque, leaving many anatomical details.

The identification of intracranial anatomical structures is not only based on direct observation but also through certain markers such as orifices and channels.

Several parts of the brain could be identified on CT images: the frontal, parietal, temporal and occipital lobes of each cerebral hemisphere were clearly identified on the cross sections and on the median section.

On the median cut, as well as on cross sections, the hypothalamus (Figure 4/13), the cavernous sinuses (Figure 4/14, 5/11), the midbrain (Figure 5/9, 8/14), and myelencephalon (Figure 8/12) are clearly visualized. The cerebellum with its components, vermis and cerebellar lobes are easily identifiable (Figure 7, 8).

The olfactory bulbs are clearly visible and well circumscribed; they are separated by the perpendicular plate of the ethmoid bone (Figure 1/6).

As for the encephalic ventricles, the third (Figure 4/9, 5/8, 6/7) is clearly visible, the lateral ventricle (Figure 4/10, 5/7) and the fourth one are discernible. This could be explained by the fact that it is a corpse and therefore the ventricular edges have collapsed.

The mesencephalic aqueduct was not visible on CT. Similarly, most of the brainstem nuclei were not identified on CT.

With CT imaging, the brain shows a homogeneous appearance which makes it difficult to separate different tissues. Particularly, the subarachnoid spaces, the gray matter and the white substance are unidentifiable.

In this study, there was not a clear distinction between the encephalon's ventricular cavities. However, CT scanning of live animals can visualize and identify them, as confirmed by the work of Hathcocket al (1995) and Probst et al (2005).

Interestingly, CT image's accuracy and sharpness vary depending on the spacing technique used. This study agrees with previous findings that lower slice thickness increase CT image details (Marwan and Norlaili 2017; Katkar et al. 2016; Yao et al. 2016). Although, thinner slices increase image noise, small lesion's visibility was improved by providing more diagnostic content (Nagel 2007).

Computed tomography images could not visualize any nerve. Gonçalves et al. (2015) were able to identify several cranial nerves by MRI on the horse's head by following the path and ramifications of several nerves. The same authors note that CT images only identify the emergence foramen of these cranial nerves.

3.2.2. Surrounding structures

Both meninges and the venous sinus couldn't be identified on CT.

The whole skeleton of the craniofacial massif as well as the bones of the mandible and the hyoid apparatus are very clear and easily identifiable. Thus, there is a strong correlation between the anatomical sections and the corresponding CT images with the finest details. The frontal (Figure 1/1, 2/1, 3/2, 4/2), parietal (Figure 3/6, 4/4, 7/6, 8/4), temporal (Figure 5/12, 6/12), sphenoid (Figure 3/22, 4/16), basisphenoid (Figure 5/18, 6/18) and the occipital (Figure 8/3) bones are well identified.

The surrounding soft tissues appear with an intermediate degree of attenuation. Differentiation between muscles, salivary glands, fat, tongue and mucosal surfaces is difficult. For example, the oculomotor muscles cannot be identified within the periorbital fat. However, some soft structures like the masticatory muscles, tongue, and soft palate have been identified through their relationship to bone structures and cavities.

Air cavities are easily visualized in CT images. Thus, the nasopharynx (Figure 1/12, 2/18, 3/24, 6/19), the oropharynx (Figure 8/40), the oral cavity (Figure 5/26, 8/35), the bone sinuses frontal (Figure 1/3/4/5) sphenoidal (Figure 2/16) cavernous (Figure 4/14, 5/11, 6/11) and buccal cavity (Figure 4/23, 5/22, 6 / 17), are clearly visible. All these cavities appear in black because they have a low degree of attenuation.

Most important vascular ducts observed such us the mandibular alveolar artery and vein (Figure 3/32), the maxillary artery and vein (Figure 3/14), the external jugular vein (Figure 7/24), the common carotid artery (Figure 7/26) and many other peripheral vessels appear with a low degree of attenuation, and can be differentiated from surrounding structures.

3.3. Magnetic resonance imaging

3.3.1. Brain

The T1-weighted MRI sequences helped identify most of the brain's anatomical structures through the excellent contrast obtained between both gray and white matters and the ventricles. This leads to an excellent correspondence between MRI images and anatomical cross sections.

In T1-weighted images, adipose tissue and bone marrow generate a high signal, whereas muscles and other soft tissues (glands, nerves, cerebral parenchyma…) demonstrate an intermediate signal. The signal of the white substance is slightly more hyperintense compared to the signal of the gray matter. Vascular structures, cerebrospinal fluid and air show an empty signal. Only bone structures of the skull, which show a signal gap on the MRI images, could be better visualized on the cross sectional images.

The surface of the cerebral convolutions and cerebral fissures are easily distinguishable in all images, as well as the deepest structures such as the myelencephalon (Figure 8/12), the pons (Figure 8/13), the cerebellar vermis (Figure 7/8), the midbrain (Figure 5/9, 8/14), the thalamus (Figure 4/8), the hypothalamus (Figure 4/13) and the pituitary gland (Figure 4/15).

The cerebrospinal fluid included in the encephalic ventricle system and the subarachnoid spaces have negligible signal intensity, so they appear in black. We can easily identify the cerebral ventricles, the lateral (Figure 5/10, 6/7), the third ventricle (Figure 4/9, 5/8, 6/7) and the fourth ventricle (Figure 8/28).

The cranial nerves are also easily identifiable with MRI, We were able to identify the optic nerve (Figure 2/9, 3/13), the maxillary nerve (Figure 3/14) and the mandibular alveolar nerve (Figure 3/32).

While with MRI, the white substance appears gray and has more signal intensity than bones, the gray matter is more intense than the white substance with a slight gray. The ventricular system appears black with a low intensity signal. The T1 weighting chosen provides a good contrast between the gray matter and the white matter,Parizel et al. (2010) make the same observation. Mogicato et al. (2011) mentioned that this sequence provides good spatialization of resolution and better anatomical contrast for identifying fine structures on MRI images.

3.3.2. Surrounding structures

On the MRI images, we could not identify the venous sinus and meninges. Moreover, the bones are visualized indirectly via the bone marrow's fat. The skull, and bones of the face are highlighted by the observation of the area of the hypo-intense signal corresponding to the bones' cortical margins.

All the structural components of the temporomandibular joint, joint cavity, synovial fluid, ligaments and joint disc are easily identifiable. They are exactly comparable to the structures identified on transverse anatomical sections made through the temporomandibular joint (Figure 4/21, 5/15, 6/14).

The head's muscles have intermediate signal intensity and appear gray. All the masticatory muscles (temporal, medial and lateral pterygoid, masseter and digastric) were identified, as well as certain motor muscles of the tongue, hyoid apparatus and soft palate.

Other surrounding soft tissue structures, such as salivary glands (Figure 1/28, 6/16), mucosal surfaces, soft palate (Figure 3/26, 4/28,), and tongue (Figure 1/25, 2/27, 8/36/38/39) have a low intensity and appear gray, relative to the cranial bones. They are easily recognizable on MRI images and correspond perfectly to anatomical sections.

Air cavities are well defined on MRI images. The frontal sinus (Figure 1/3/4/5), the sphenoidal sinus (Figure 2/16), the oral venous sinus (Figure 4/23, 5/22, 6/17), the nasopharynx (Figure 1/12) , 2/18, 3/24, 6/19), the oropharynx (Figure 8/40), the oral cavity (Figure 5/26, 8/35) and the laryngo-pharynx (Figure 8/43) appear at low intensity relative to the associated mucosal surfaces observed with an intermediate intensity which makes them easy to identify.

3.4. Comparative study

In our study, CT and MRI have been shown to be poor at visualizing the meningeal envelopes.According to Dietemann et al. in 2005 only the falxcerebri and tentorium cerebelli are visualized on CT. Their visualization is only possible on MRI after injection of contrast medium, linked to the absence of a hemomeningeal barrier. This treatment will show meninges in the shape of a hyperintense borderline.

The use of CT as a high spatial resolution imaging technique allowed defining the finest bone structures. We obtained detailed images of the skull, mandible and hyoid bones, with a high degree of attenuation, so that clear differentiations could be made between cortical and bone marrow. Thus, changes in density, fractures, and abnormalities in the position of the false brain are easily identified on CT images.

Skull bones have a weak signal intensity and appear black on MRI. We were only able to identify them indirectly through bone marrow fat, as well as by observation of the bones. Hypo-intense areas correspond to the cortical margins of these bones.

Surrounding soft tissues' structures, such as muscles, tongue, salivary glands and associated mucosal surfaces of the pharynx and larynx, appear with an intermediate degree of attenuation which makes them hard to be identified on the CT images. However, boundaries between the different structures are clear on MRI.

The different air cavities are easy to visualize with both CT and MRI. Interestingly, we also noticed the presence of air in some vessels, which could be well attributed to post-mortem changes, as described by Morrow et al. (2000).Very few studies focused on exploring the dromedary's encephalon with new imaging methods. To our knowledge, this is the first study where anatomical sections, CT and MRI were used to explore the dromedary's encephalon. High quality images were obtained with a good correspondence between the anatomical sections in both CT and MRI images.

Overall, the complex anatomy of the dromedary's head, particularly the brain is better defined by MRI. This is due to the fact that MRI has the ability to produce two-dimensional images of the brain in very detailed and highly contrasted gray levels, non-invasively and without ionizing forms of electromagnetic energy.

We confirmed that MRI is better in detecting and evaluating intracranial anatomical structures because it provides better image quality and finer details. Indeed, the important contrasts between different structures of the encephalon offered by the MRI enabled us to visualize important anatomical detail from all of the brain's structures. Moreover, the MRI provides a better distinction between bone and soft tissue compared to other imaging modalities (Arredondo et al. 2013, Aiken et al. 2012, Bag et al. 2014, Ikeda and Ikeda 2016).

Le Blanc and Daniel (2007) showed that MRI is preferable for caudal cerebral fossa structures since these are often poorly defined in CT images. This is due to the drag artifacts in CT resulting from hardening of the beam in this region.

Several brain structures such as the gray matter, white matter, inner capsule, optic chiasm, hippocampus convolutions, cerebral peduncles, bridge, choroidal plexus, vermis, and paraflocculus of the cerebellum are easily discernable with MRI while they are virtually unidentifiable on CT. This is because it provides better resolution of brain parenchyma, fewer artifacts particularly in the infratentorial brain region (Heinrich and Jochen 2015).

On the other hand, skeletal structures of the skull, especially the bones, foraminae, pits and canals, are more distinct on the CT images.

CT allows us to visualize bone structures, the brain and surrounding structures, such as soft tissue under a bone structure. This medical imaging technique has a high resolving power that makes it possible to differentiate certain parenchymal structures of the head from one another in addition to differentiating them from liquids and gas. We join Morrow et al. (2000) and De Zani et al. (2010) to say that CT provides excellent spatial resolution and good bone-soft tissue discrimination in the head.

The MRI machine used for this study had a magnetic fields intensity of 3 Tesla. A higher magnetic field machine (7 Tesla) would have certainly improved the quality of MRI images and given us more details about anatomical structures. Anja et al. in 2017 showed that the clinically established increase of the field strength from 1.5 to 3 Tesla offered imaging at increased spatial resolution with comparable image quality and no relevant exacerbation of artifacts. Further increase of the field strength to 7 Tesla demonstrated its high imaging potential.

It would also be interesting to deepen our work by using specific techniques for imaging brain vessels such as cerebral CT angiography or magnetic resonance angiography (MRA) to detect the specific peculiarities of irrigation of the dromedary encephalon.

Unfortunaltely, the use of MRI and CT as a unique diagnostic imaging modality is generally limited in veterinary practice, particularly for large animals such as camels (Arencibia et al. 2005; Arencibia et al. 2012; Nawal and Elkarmoty 2018). In Tunisia, some experimental work has been done on cadaveric anatomical parts but not on live animals. This difficulty is mainly due to the lack of a specialized center for veterinary medical imaging.

4. Conclusion

Our work confirms that CT is superior to MRI for fine bone tissue and any structural changes or bone density, while MRI is superior in assessing soft tissue, brain cavities and surrounding soft structures.

The confrontation between anatomical sections from both CT and MRI helped us better understand the topography of the normal structure of the dromedary's encephalon; it also offered stereotaxic precisions that can be used to diagnose tumoral or degenerative pathologies. Future studies could focus on comparing CT and MRI appearance of the camel's head on both juvenile and adults are necessary to compare normal relative positions and anatomical structure sizes as a function of age.

Acknowledgements
We would like to thank doctors Rajhi Hatem and Moulahihassen, radiologists doctors for their supervision during the realization of the tomodensitometry and magnetic resonance imaging, MrLotfiChihaoui; the technician of the anatomy department of the National School of Veterinary Medicine of SidiThabet for his help in the anatomical sections.

Conflict Of Interest Statement
To the Editorial Board of Journal of New Science
On behalf of all the authors, I hereby state a) that the paper has not been submitted for publication elsewhere, b) that there are no financial or any other types of relationships that might lead to a conflict of interests, and c) that the manuscript has been read and approved by all authors.
Thank you in advance for your consideration.

References

Aiken A, Bouloux G, Hudgins P (2012)MR Imaging of the temporomandibular joint. *Magnetic Resonance Imaging Clinics of North America*,**20**:397–412. doi:10.1016/j.mric.2012.05.002

Anja L, Karsten B, Oliver K, Stefan M, Karsten W, Mark E L, Thomas C L, Michael F, Harald H Q, Kai N,Lale, U (2017) 1.5 versus 3 versus 7 Tesla in abdominal MRI: A comparative study. *PLOS ONE* | https://doi.org/10.1371/journal.pone.0187528 N

Arencibia A, Rivero M A, Gil F, Ramirez J A, Corbera J A, Ramirez G, Vasquez J M (2005) Anatomy of the cranioencephalic structures of the camel (*Camelusdromedarius*) by imaging techniques: a Magnetic Resonance Imaging study. *Anatomia. Histolologia. Embryologia*, **34**, 52-55. doi : 10.1111/j.1439-0264.2004.00572.x

Arencibia A, Blanco D, González N, Rivero M A (2012) Computed tomography and magnetic resonance imaging features of the temporomandibular joint in two normal camels. *Anatomy Research International*, 1–6.doi: 10.1155/2012/242065

Arredondo J, Agut A, Rodríguez M J, Sarriá R, Latorre R(2013)Anatomy of the temporomandibular joint in thecat: a study by microdissection, cryosectionandvascular injection. Journal of Feline Medicine and Surgery, 15:111–116.doi: 10.1177/1098612X12462704.

Bag A K, Gaddikeri S, Singhal A, Hardin S, Tran B D, Medina J A, Curé J K (2014) Imaging of the temporomandibular joint: an update. *World Journal of Radiology*, **6**:567–582. doi: 10.4329/wjr.v6.i8.567

Blanco D, Vazquez J M, Riveroa M A, Corberac J A, Arencibia A (2015) Computed tomography of the brain and associated structures of the one-humped camel (*Camelusdromedarius*): an anatomic study. *Journal of Applied Animal Research*, Vol. 43, No. **2**, 218–223. doi:10.1080/09712119.2014.963092

Byers S R, Parish S M, Holmes S P, Donahoe S L, Barrington G M (2007) A fungal granuloma of the frontal sinus in a llama. *Canada Veterinary Journal*, **48**: 939-941.

De Rycke L (2007) Magnetic Resonance imaging of the Normal Canine Brain in *Correlative Computed Tomography, Magnetic Resonance Imaging and Cross-sectional Anatomy of Selected Regions of the Canine Body*, CHAPTER 1.1.2, page 105-118

De Zani D, Borgonovo S, Biggi M, Vignati S, Scandella M, Lazzaretti S, Modina S., Zani D (2010) Topographic comparative study of paranasal sinuses in adult horses by computed tomography, sinuscopy, and sectional anatomy. *Veterinary Research Communications* **34**, 13-16.doi: 10.1007/s11259-010-9381-6

Dietemann J L, Correia Bernardo R, Bogorin A, Abu Eid M, Koob M, Nogueira T, Vargas M I, Fakhoury W, Zöllner G (2005) Normal and abnormal meningeal enhancement: MRI features. *Journal de radiologie*, Vol**86**, N 11-pp. 1659-1683. doi : JR-11-2005-86-11-0221-0363-101019-200506073

Gonçalves R, Malalana F, Mc Connell J F, Maddox T (2015) Anatomical study of cranial nerve emergence and skull foramina in the horse using magnetic resonance imaging and computed tomography. Veterinary Radiology and Ultrasound**,** 56(4):391-7. doi: 10.1111/vru.12256

Hathcock J T, Pugh D G, Cartee R E, Hammond L (1995) Computed tomography of the llama head: technique and normal anatomy. *Veterinary Radiology and Ultrasound*. **36**:290–296. doi :10.1111/j.1740-8261.1995.tb00265.x

Heinrich J A, Jochen B F (2015) Brain Imaging in Acute Ischemic Stroke—MRI or CT?.*Current Neurolology and Neuroscience Reports*. 15:6. doi: 10.1007/s11910-015-0526-4

Ikeda R, Ikeda K (2016). Directional characteristics of incipient temporomandibular joint disc displacements: a magnetic resonance imaging study. American Journal of Orthodontics and Dentofacial Orthopedics, **149**:39–45.doi: 10.1016/j.ajodo.2015.06.021.

Le Blanc A K, Daniel G B, (2007) Advanced imaging for veterinary cancer patients. *Veterinary Clinics of North America. Small Animal Practice*, **37**: 1059-1077. doi : 10.1016/j.cvsm.2007.06.004

Marwan A, Norlaili A K (2017) Effect of slice thickness on image noise and diagnostic content of single-source-dual energy computed tomography. *Journal of Physics.* Conference. Series. 851 012005. doi:10.1088/1742-6596/851/1/012005

Mogicato G, Conchou F, Raharison F, Sautet J (2011) Normal canine brain: comparison between magnetic resonance imaging and crosssectional anatomy. *Revue de Médecine vétérinaire.***162**, 8-9, 400-405.

Morrow K L, Park R D, Spurgeon T L, Stashak T S,Arceneaux B (2000) Computed tomographic imaging of the equine head. *Veterinary Radiology and Ultrasound*, **41**:491–497. doi : 10.1111/j.1740-8261.2000.tb01876.x

Nagel HD (2007) CT parameters that influence the radiation dose, in Radiation dose from adult and pediatric multidetector computed tomography. Springer. p. 51-79.doi: 10.1007/978-3-540-68575-3_4

Nawal A N, Elkarmoty F (2018) Anatomical, Radiographical and Magnetic Resonance Imaging features of normal Temporomandibular Joint (TMJ) in camels (*Camelusdromedarius*): A special reference to TMJ surgical approach. *International Journal of Advanced. Research in BiologicalSciences.***5** (2): 34-43. doi : 10.22192/ijarbs

Osuobeni E P, Hamidzada W A (1999) Ultrasonographic determination of the dimensions of ocular components in enucleated eyes of the one-humped camel (*Camelusdromedarius*). *Research in Veterinary Science*, **67**: 125-129. doi :10.1053/rvsc.1998.0288

Parizel P M, Van Den Hauwe L, Belder FD, Van Goethem J, Venstermans C, Salgado R (2010) Magnetic resonance imaging of the brain. *In:* Clinical MR Imaging, Reimer, P., Parizel, P. M., Meaney, J. F. M. and Stichnoth, F. A. (Eds.). Springer-Verlag, Berlin, Heidelberg. pp 110-112.

Probst A, Henninger W, Willmann M (2005) Communications of normal nasal and paranasal cavities in computed tomography of horses. *Veterinary Radiology and Ultrasound.***46**:44–48. doi : 10.1111/j.1740-8561.2005.00008.x

Katkar R, Steffy D D, Noujeim M, Deahl ST, Geha H (2016) The effect of mA, number of basis images and export slice thickness on contrast-to-noise ratio and detection of mandibular canal on cone beam computed tomography scans: an in vitro study. *Oral Surgery, Oral Medicine, Oral Pathology and Oral Radiology*.doi: 10.1016/j.oooo.2016.08.006.

World Association of Veterinary Anatomists (2012) Nominaanatomicaveterinaria. 5th edition (Revised version). Vienna, Austria: International Committee on Veterinary Anatomical Nomenclature.

Yao Y, Ng JM, Megibow AJ, Pelc NJ (2016) Image quality comparison between single energy and dual energy CT protocols for hepatic imaging. *Medical Physics*. **43**(8): p. 4877-4890.doi: 10.1118/1.4959554.

Figure And Legends

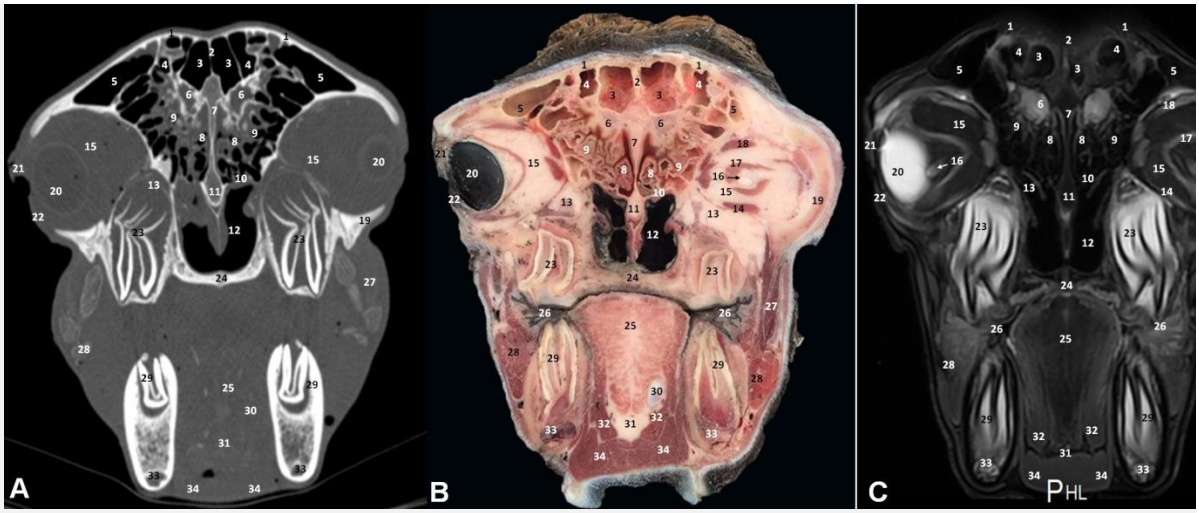

Figure 1: Cross sections through the olfactory bulb (A: Bone window CT image; B: anatomic section ; C: T1-weighted MR image). 1. Frontal bone; 2. Median septum of the frontal sinuses; 3. Caudal frontal sinus; 4. Medial frontal sinus; 5. Lateral frontal sinus; 6. Olfactory bulb; 7. Perpendicular blade of the ethmoid bone; 8. Endoturbinal volutes of ethmoid bone; 9. Ectoturbinal volutes of ethmoid bone; 10. Papyraceous lamina; 11. Vomer bone; 12. Pars nasalispharyngis; 13. Infra-orbital fat; 14. Ventral rectus muscle; 15. Orbital fat; 16. Optic nerve; 17. Dorsal rectus muscle; 18. Levatorpalpebraesuperiosis; 19. Zygomatic process of temporal bone; 20. Iris; 21. Upper eyelid; 22. Lower eyelid; 23. Upper third molars M3; 24. Horizontal blade of palatal bone; 25. Lingual septum; 26. Palate diverticulum; 27. Masseter muscle; 28. Mandibular salivary gland; 29. Lower third molar M3; 30. Hyoid bone; 31. Tongue fat; 32. Mylohyoid muscle; 33. Root pulp; 34. Geniohyoid muscle

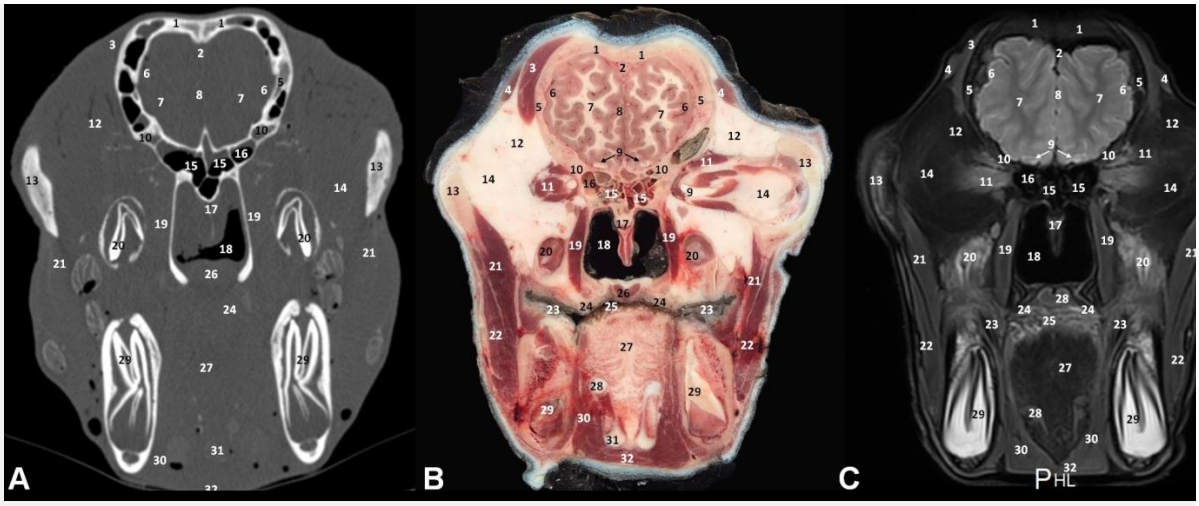

Figure 2: Cross sections through the frontal lobe (A: Bone window CT image; B: anatomic section; C: T1-weighted MR image). 1. Frontal bone; 2. Dorsal sagittal sinus; 3. Temporal muscle; 4. Auricular muscle; 5. Parietal bone; 6. Parietal lobe of the brain; 7. Semioval center; 8. Cerebral longitudinal fissure; 9. Optic nerve; 10. Sphenoïd bone; 11. Levatorpalpebraesuperiosis; 12. Supra orbital fat; 13. Zygomatic process of temporal bone; 14. Orbital fat; 15. Endoturbinal volutes of ethmoid bone; 16. Sphenoid sinus; 17. Vomer bone; 18. Pars nasalispharyngi; 19. Medial pterygoideus muscle; 20. Root pulp; 21. Deep part of the masseter muscle; 22. Superficial part of the masseter muscle; 23. Palate diverticulum; 24. Palatine glands; 25. Oral cavity; 26. Soft palate; 27. Tongue; 28. Stylohyoid bone; 29. Lower third molar M3; 30. Mylohyoid muscle; 31. Thyrohyoid bone; 32. Geniohyoid muscle

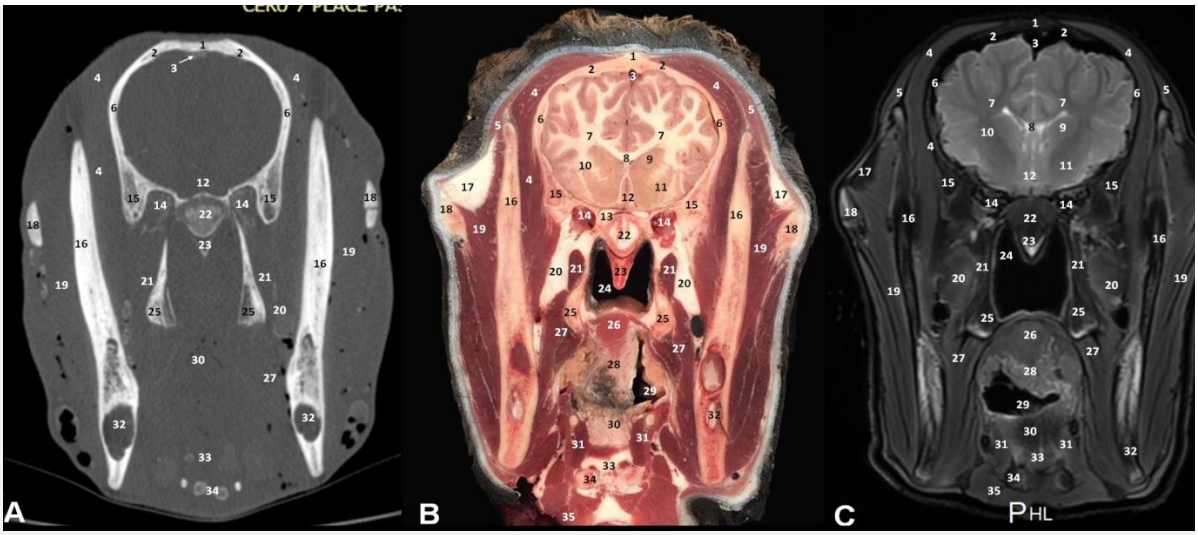

Figure 3: Cross sections through the optic chiasm (A: Bone window CT image; B: anatomic section; C: T1-weighted MR image): 1. External sagittal crest; 2. Frontal bone; 3. Dorsal sagittal sinus; 4. Temporal muscle; 5. Zygomaticoauricularis muscle; 6. Parietal bone; 7. Semioval center; 8. Corpus callosum; 9. Caudate nucleus; 10. Internal capsule; 11. Putamen; 12. Interthalamic adhesion; 13. Optic nerve; 14. Maxillary artery vein and nerve; 15 Greater wing of the sphenoid bone; 16. Ramus of mandible; 17. Retro orbital fat; 18. Zygomatic process of temporal bone; 19. Masseter muscle; 20. Fat body; 21. Lateral pterygoideus muscle; 22. Body of basisphenoid bone; 23. Sphenoid ridge; 24. Pars nasalispharyngis; 25. Perpendicular plate of palatine bone; 26. Soft palate; 27. Medial pterygoideus muscle; 28. Palatine glands; 29. Oral cavity; 30. Tongue; 31. Mylohyoid muscle; 32. Inferior alveolar nerves; 33. Hyoid bone; 34. Thyrohyoid muscle; 35. Geniohyoid muscle

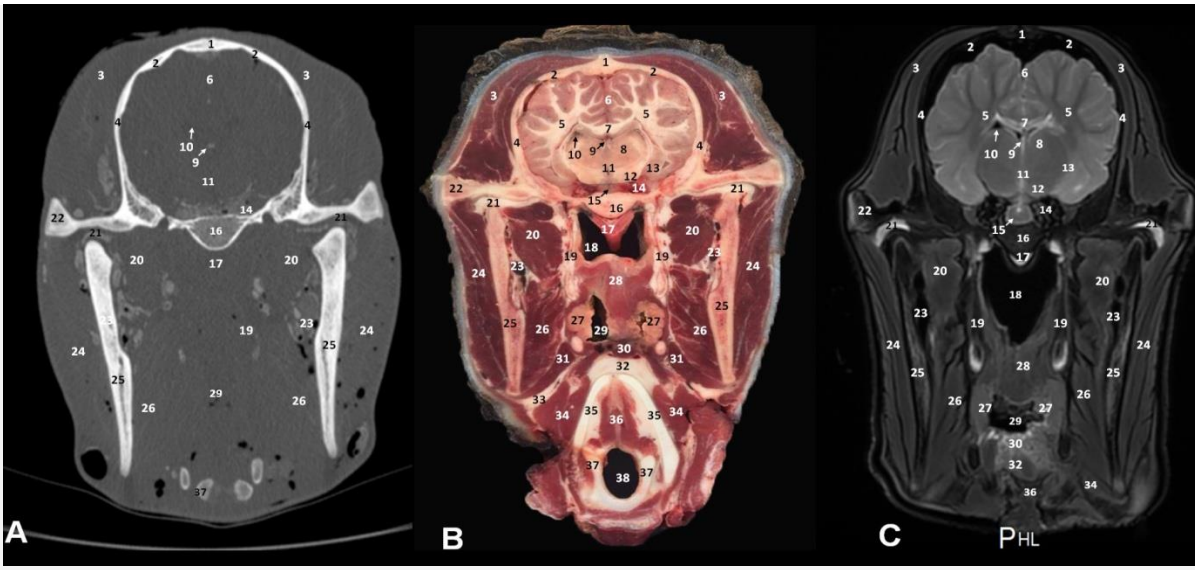

Figure 4: Cross sections through the pituitary gland (A: Bone window CT image; B: anatomic section; C : T1-weighted MR image): 1. External sagittal crest; 2. Parietal bone; 3. Temporal muscle; 4. Temporal bone; 5. Semioval center; 6. Cerebral longitudinal fissure; 7. Corpus callosum; 8. Thalamus; 9. Third ventricle; 10. Lateral ventricle; 11. Mesencephalic aqueduct (Sylvius); 12. Cerebral peduncle; 13. Hypothalamus; 14. Cavernous sinus; 15. Hypophysis; 16. Body of basisphenoid bone; 17. Sphenoid ridge; 18. Pars nasalispharyngis; 19. Perpendicular plate of palatine bone; 20. Lateral pterygoideus muscle; 21. Temporomandibular joint; 22. Zygomatic process of temporal bone; 23. Sinus of the oral vein; 24. Masseter muscle; 25. Ramus of mandible; 26. Medial pterygoideus muscle; 27. Palatine glands; 28. Soft palate; 29. Pars oralispharyngis; 30. Pharynx; 31. Mylohyoid muscle; 32. Pharyngo-basilar fascia; 33. Pterygoid fascia; 34. Thyro-arytenoid muscle; 35. Arytenoid cartilage; 36. Transverse arytenoid muscle; 37. Thyroid cartilage; 38. Laryngeal cavity; 39. Hyoid bone

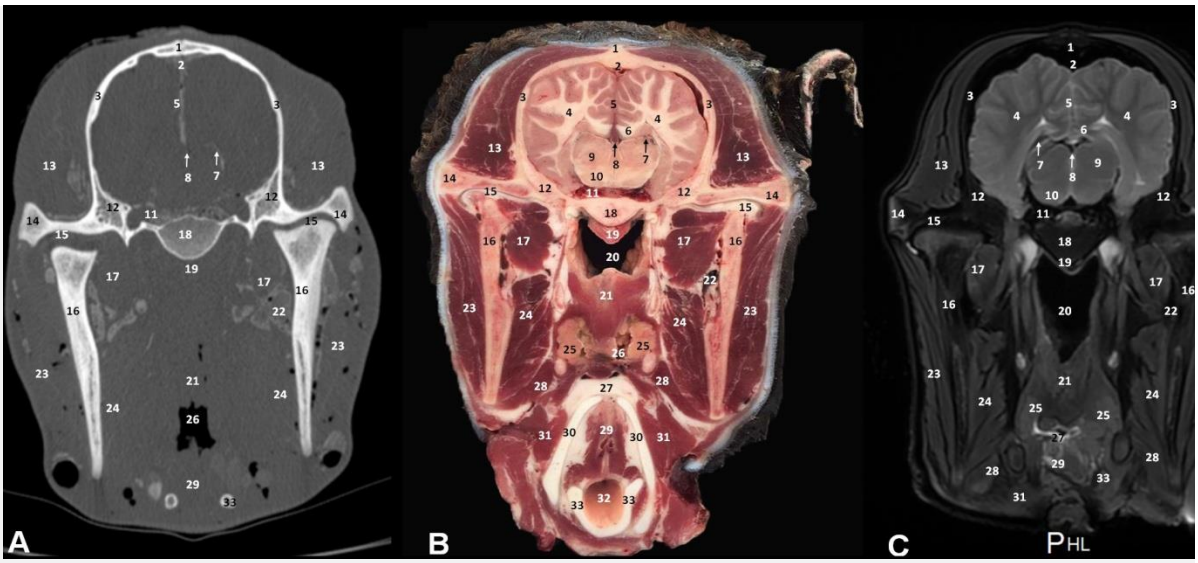

Figure 5: Cross sections through the cerebral peduncle (A: Bone window CT image; B: anatomic section; C: T1-weighted MR image): 1. External sagittal crest; 2. Dorsal sagittal sinus; 3. Parietal bone; 4. Semioval center; 5. Cerebral longitudinal fissure; 6. Corpus callosum; 7. Lateral ventricle; 8. Third ventricle; 9. Mesencephalon; 10. Cerebral peduncle; 11. Cavernous sinus; 12. Temporal bone; 13. Temporal muscle; 14. Zygomatic process of temporal bone; 15. Temporomandibular joint; 16. Ramus of mandible; 17. Lateral pterygoideus muscle; 18. Basisphenoid bone; 19. Sphenoid ridge; 20. Pars nasalispharyngis; 21. Soft palate; 22. Sinus of the oral vein; 23. Massetermuscle; 24. Medialpterygoideusmuscle; 25. Palatine glands; 26. Pars oralispharyngis; 27. Pharyngo-basilar fascia; 28. Mylo-hyoid muscle; 29. Transverse arytenoid muscle; 30. Arytenoid cartilage; 31. Thyro-arytenoid muscle; 32. Laryngeal cavity; 33. Thyroid cartilage

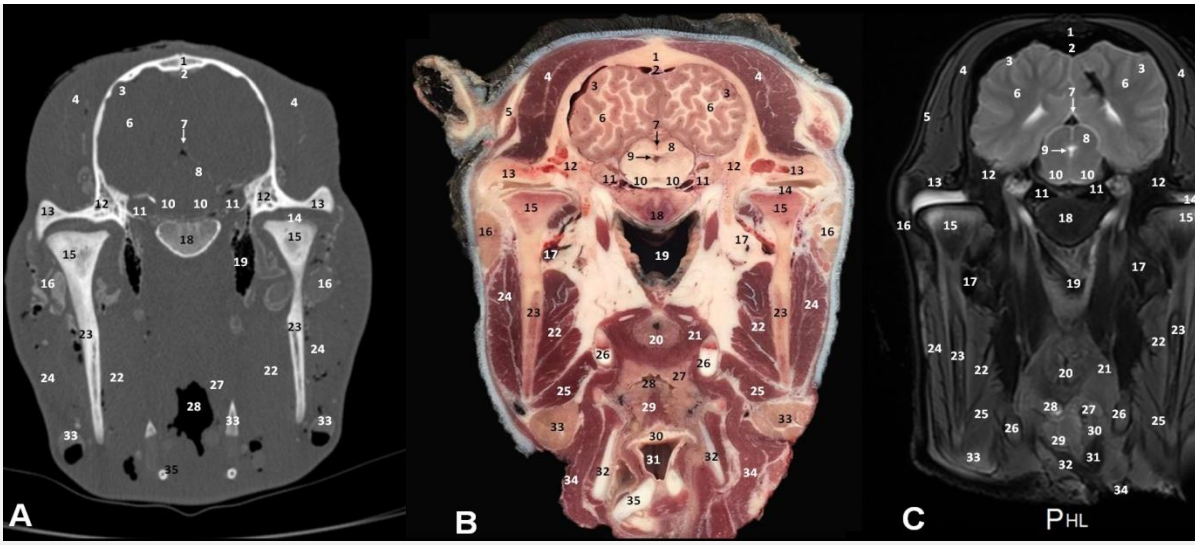

Figure 6: Cross sections through the mesencephalic aqueduct (A: Bone window CT image; B: anatomic section; C: T1-weighted MR image): 1. External sagittal crest; 2. Dorsal sagittal sinus; 3. Cerebral cortex; 4. Temporal muscle; 5. Scutiform cartilage; 6. Semioval center; 7. Third ventricle; 8. Rostral colliculus; 9. Mesencephalic aqueduct; 10. Cerebral peduncle; 11. Cavernous sinus; 12. Temporal bone; 13. Zygomatic process of temporal bone; 14. Temporomandibular joint; 15. Articular process of the mandible; 16. Mandibular salivary glands; 17. Sinus of the oral vein; 18. Basisphenoid bone; 19. Pars nasalispharyngis; 20. Soft palate; 21. Palatopharyngeal muscle; 22. Medial pterygoideus muscle; 23. Ramus of mandible; 24. Masseter muscle; 25. Mylohyoid muscle; 26. Stylohyoid bone; 27. Palatine glands; 28. Pars oralispharyngis; 29. Tongue; 30. Palate-pharyngeal arch; 31. Laryngeal cavity showing the vocal cords; 32. Arytenoid cartilage; 33. Mandibular lymph nodes; 34. Hyothyroid muscle; 35. Thyroid cartilage

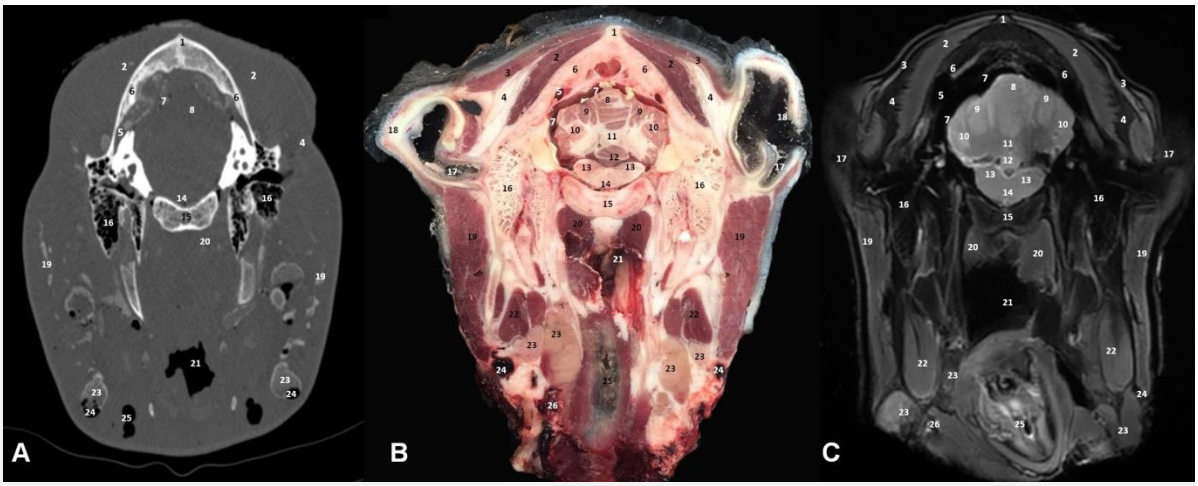

Figure 7: Cross sections through the cerebellum (A: Bone window CT image; B: anatomic section; C: T1-weighted MR image): 1. External sagittal crest; 2. Temporal muscle; 3. Interscutularis muscle; 4. Scutiform cartilage; 5. Dorsal venous sinus; 6. Parietal bone; 7. Subarachnoid space; 8. Folium vermis; 9. Ansiform lobe of the cerebellum; 10. Paraflocculus; 11. Cerebellar medulla; 12. Nodulus of vermis; 13. Medulla oblongata; 14. Medullary pyramids; 15. Basioccipital bone; 16. Petrous part of temporal bone; 17. External auditory canal; 18. Auricularcartilage; 19. Massetermuscle; 20. Longus capitismuscle; 21. Piriformrecess; 22. Digastricmuscle; 23. Retropharyngeallymphnodes; 24. Externaljugularvein; 25. Esophagus; 26. Common carotid artery

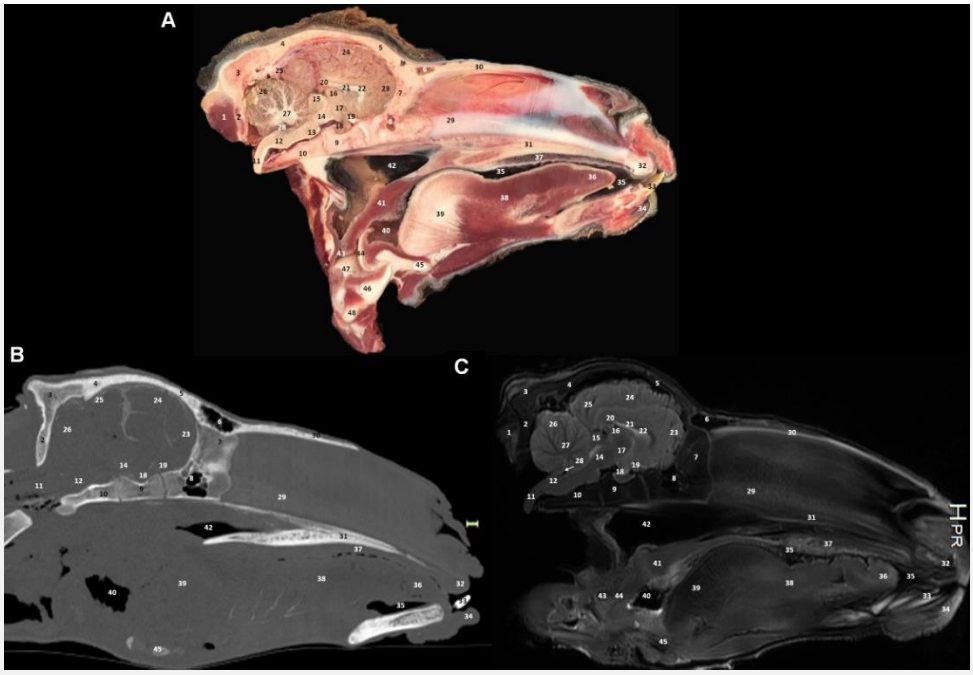

Figure 8: sagittal sections of the head (A: anatomic section; B: bone window CT image; C: T1-weighted MR image): 1. Semispinaliscapitis; 2. Occipital condyle; 3. Occipital bone; 4. Parietal bone; 5. Frontal bone; 6. Frontal sinus; 7. Ethmoid bone; 8. Sphenoid sinus; 9. Basisphenoid bone; 10. Basioccipital bone; 11. Spinal cord; 12. Medulla oblongata; 13. Pons; 14. Mesencephalon; 15. Rostral Colliculus; 16. Epithalamus; 17. Thalamus; 18. Hypophysis; 19. Optic chiasm; 20. Splenium of corpus callosum; 21. Body of corpus callosum; 22. Genu of corpus callosum; 23. Frontal lobe; 24. Parietal lobe; 25. Meninges; 26. Cerebellum; 27. Arbor vitae; 28. Fourth ventricle; 29. Nasal septum; 30. Nasal bone; 31. Hard palate; 32. Dental pad; 33. Lower incisor; 34. Upper lip; 35. Oral cavity; 36. Apex of the tongue; 37. Rugae of hard palate; 38. Body of the tongue; 39. Root of the tongue; 40. Pars oralispharyngis; 41. Soft palate; 42. Pars nasalispharyngis; 43. Laryngopharynx; 44. Epiglottis; 45. Hyoid bone; 46. Thyroid cartilage; 47. Arytenoid cartilage; 48. Cricoid cartilage